COBEM 2023 27TH INTERNATIONAL CONGRESS OF MECHANICAL ENGINEERING

ABCM Brazilian Society of Mechanical Sciences and Engineering
27th ABCM International Congress of Mechanical Engineering
December 04-08, 2023, Florianópolis-SC, Brazil

# COB-2023-0697
# A CFD STUDY ON AIRFOILS PERFORMANCE IN FORMULA SAE

**Josue Lima de Camargo**
**Marcos Vinicius Barbosa**
Department of Mechanics, Federal University of Technology – Paraná, Ponta Grossa, PR 84017-220, Brazil
josuelima@alunos.utfpr.edu.br, mvbarbosa@utfpr.edu.br

***Abstract.*** *The present study conducts an analysis on the aerodynamic performance of the S1223 and Be122-125 airfoil profiles in a single-element configuration with a chord length of 0.400m for two-dimensional airflows at typical Reynolds numbers for Formula SAE (300 000, 400 000 and 800 000). The investigation employs Computational Fluid Dynamics (CFD) simulations by utilizing the Transition SST model available within the Ansys® Fluent 2021 R2 software in order to obtain the coefficients of lift, drag, pressure and skin-friction as output variables. The objective is to achieve maximum downforce generation while reducing the stall rate, thereby attaining the desired performance. In this regime, the flow conditions are categorized as "low Reynolds", which is characterized by the development of a recirculation zone named as Laminar Separation Bubble that can potentially lead to lift losses. The S1223 airfoil outperformed in terms of both downforce generation and stall rate, with the latter being evaluated using the criteria of turbulent separation position and the movement of transition location towards the leading edge.*

***Keywords:*** *airfoils, CFD, FSAE, laminar separation bubble, Transition SST.*

## 1. INTRODUCTION

The motorsports world underwent a Revolution in the late 1960s by introducing the use of wings as a way to optimize performance in professional racing. On a reduced scale, but introductory to the topic in the university environment, Formula SAE (FSAE) represents an opportunity to deal with such aspects as a prototype designer, with the primary objective for aerodynamics being the generation of downforce. In this context, Computational Fluid Dynamics (CFD) tools are of fundamental importance for a pre-manufacturing analysis of what will actually have practical effects.

The low characteristic velocities observed in competition categorize the flow as “low Reynolds”, where the primary phenomenon involved is the transition induced by separation with the formation of a recirculation zone called the Laminar Separation Bubble (LSB). This can lead to substantial alterations in the pressure distribution across the airfoil, consequently negatively impacting its performance (Gad-el Hak, 1990).

The present study analyzes the behavior and properties of external, incompressible and two-dimensional airflows over wing profiles of interest through CFD simulations for a single element configuration with a chord-length ($c$) of 0.400 m, a typical size for FSAE vehicles. The airfoils used for the prototype should preferably have design characteristics that promote high value of maximum lift associated with a reduced stall rate, which makes the S1223 and Be122-125 airfoils compatible with the objective and the chosen subjects for further investigation.

In order to calculate low Reynolds number external flows, a robust numerical method capable of predicting separation-induced transition must be employed. Therefore, simulations were performed using the Transition SST model available in Ansys® Fluent 2021 R2 software on the aforementioned airfoils at chord-based Reynolds values of $3{\cdot}10^5$, $4{\cdot}10^5$ and $8{\cdot}10^5$, which correspond to the characteristic speeds of dynamic events in FSAE competition (SAE International, 2022). The desired output variables are the lift coefficient ($C_l$), drag coefficient ($C_d$), pressure coeficient ($C_p$) and skin-friction coefficient ($C_f$). The results obtained will be discussed and compared to determine which airfoil profile exhibits the best performance.

## 2. LITERATURE REVIEW

### 2.1 Laminar Separation Bubble

Gad-el Hak (1990) states that an external flow is considered low Reynolds when this parameter ranges between $10^4$ and $10^6$. Within this interval, the boundary layer tends to remain laminar until the onset of adverse pressure gradient (pressure recovery), and due to its poor resistance to separation, it experiences detachment, forming a free shear layer that is highly unstable. This region is where the transition occurs. Once it becomes turbulent, the boundary layer reattaches due to increased entrainment, forming the Laminar Separation Bubble (LSB), which causes a drastic drop in aerodynamic performance.

The length and properties of the LSB depend on various factors, including the Reynolds number ($Re$), freestream

turbulence ($Tu$) and the angle of incidence ($\alpha$) (Roberts, 1980). It should be noted that the addition of destabilizing effects in the boundary layer facilitates the transition process. Thus, larger values of these mentioned parameters result in a shorter LSB length, leading the separation-induced transition to tend towards a bypass transition. A short bubble doesn't greatly affects the peak suction as determined from the potential flow around the airfoil, whereas a large bubble represents a condition of instability, with significant changes in the pressure distribution by effectively altering the shape over which the outer potential flow is developed (Gad-el Hak, 1990).

### 2.2 High-lift design at low Reynolds

Within realm of low Reynolds motorsports airfoils, Pakkam (2011) emphasizes that achieving high performance relies on securing a high $C_{l_{max}}$ for increased downforce generation. This assertion finds support in the simulations conducted by Mckay and Gopalarathnam (2002), which reveal that the prototypes equipped with aerodynamic packages set at an $\alpha$ of $C_{l_{max}}$ consistently yield the best lap times across all tested circuit configurations. Nonetheless, real-world track instabilities can introduce a significant risk of performance degradation for airfoils configured with an angular design near the stall, necessitating the consideration of their stall characteristics during profile design. According to Wortmann (1973), a transition point that gradually and slowly approaches the leading edge is associated with a reduced post-stall $C_l$ drop rate, thus indicating the desired soft stall.

To ensure high lift along with a softer stall, Selig and Guglielmo (1997) introduced the S1223 airfoil as a middle ground between two design philosophies. This airfoil strikes a balance between the concave pressure recovery distribution proposed by Liebeck (1990) and the convex distribution combined with increased aft loading, as observed in Wortmann's FX 63-137 airfoil. The resulting profile exhibits a concave pressure recovery region with smaller initial gradients, eliminating the abrupt pressure surges observed in Stratford's distribution, which leads to a moderated stall. Additionally, the aft loading constraint was relaxed to enhance lift and compensate its reduction provoked by the decrease in the concavity of its pressure distribution.

Benzing (1991) proposes that downforce generation should be combined with parameter adjustments to mitigate concurrent increases in drag. Among the series of airfoils designed for motorsport by the author, the Be122-125 profile is included and adopts his design philosophy for low speeds by positioning its maximum thickness upstream of the traditional $0.3c$ point and achieving maximum camber around $0.5c$. Benzing also asserts that the primary requirement for a profile to be employed under these conditions is to ensure a vigorous initial flow acceleration without losses of loading at the extremes.

The S1223 and Be122-125 airfoils are shown in Fig. 1, with the intentional similarity in geometric parameters between them being a selection criterion aimed at facilitating more extensive comparisons within this category of profiles.

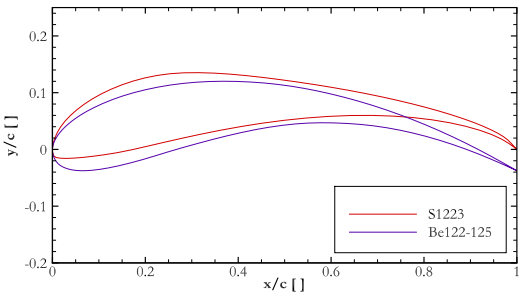

Figure 1: S1223 and Be122-125 airfoils.

### 2.3 Transition prediction with CFD

Hübbe (2017) conducted a comparative analysis between Reynolds-Averaged Navier-Stokes (RANS) turbulence models Spalart-Allmaras, $k$-$\omega$ SST, $k$-$kL$-$\omega$ and Transition SST to assess their accuracies in low Reynolds external flows over the E387 and S1223 airfoils. As expected, the first two models were not able to capture transition because they treat the flow as fully turbulent, while the $k$-$kL$-$\omega$ model overpredicted values for $C_l$, stall angle, and laminar bubble length. The Transition SST model provided better results when compared to wind tunnel data and, therefore, was chosen for the present study.

As mentioned earlier, LSBs are highly dependent on the freestream conditions. Spalart and Rumsey (2007) distinguish inflow values from ambient values (in the current case, near the wing region) due to the decay of freestream turbulence during the profile approach. The authors recommend ambient values of about $0.1\%$ for $Tu$ with the turbulent viscosity ratio ($\nu_t/\nu$) approximately equal to $2{\cdot}10^{-7}\ Re$ for typical external aerodynamics applications with SST models. In order to achieve realistic transition results, the Ansys® Fluent Theory Guide (ANSYS, 2021) suggests a low inlet value for

$\nu_t/\nu$, ranging from 1 to 10.

## 3. METHODOLOGY

### 3.1 Numerical Model

The conservation of mass (Eq. (1)) and momentum (Eq. (2)) equations, governing the flow, are:

$$\frac{\partial \rho}{\partial t} + \nabla \cdot (\rho \vec{v}) = S_m \tag{1}$$

$$\frac{\partial}{\partial t}(\rho \vec{v}) + \nabla \cdot (\rho \vec{v}\vec{v}) = -\nabla p + \nabla \cdot (\bar{\bar{\tau}}) + \rho \vec{g} + \vec{F} \tag{2}$$

where $t$ is time, $\rho$ is density, $\vec{v}$ is the velocity vector, $p$ is the static pressure, $\bar{\bar{\tau}}$ is the stress tensor, $\rho\vec{g}$ and $\vec{F}$ are the gravitational body force and external body forces, respectively, and $S_m$ is any user-defined source.

The transition predict model $\gamma$-$Re_\theta$ utilizes two transport equations with correlations based strictly on local variables and gradients, together with the wall distance. This characteristic is crucial for facilitating its implementation in modern CFD codes, which employ unstructured grids and support massive parallel execution (Menter *et al.*, 2006). The transport equation for intermittency $\gamma$ is used as a trigger for flow transition, including to solve the rapid onset of transition caused by separation of laminar boundary layers at low Reynolds. It is defined as:

$$\frac{\partial}{\partial t}(\rho\gamma) + \frac{\partial}{\partial x_j}(\rho U_j \gamma) = P_{\gamma 1} - E_{\gamma 1} + P_{\gamma 2} - E_{\gamma 2} + \frac{\partial}{\partial x_j}\left[\left(\mu + \frac{\mu_t}{\sigma_\gamma}\right)\frac{\partial \gamma}{\partial x_j}\right] \tag{3}$$

where $x_j$ is the position vector, $U_j$ is the local velocity vector, $\mu$ is dynamic molecular viscosity, $\mu_t$ is turbulent viscosity, $P_{\gamma 1}$ and $E_{\gamma 1}$ are the transition sources and $P_{\gamma 2}$ and $E_{\gamma 2}$ are the relaminarization sources. Terms assigned as $\sigma$ represent models constants.

In order to establish a connection between empirical correlations and the onset criteria in the intermittency equation, the second equation of the model was formulated in terms of the transition onset momentum-thickness Reynolds number ($\tilde{Re}_{\theta t}$). This approach enables capturing non-local influences of turbulence intensity, which vary due to the decrease in turbulence kinetic energy in the free stream and also due to the freestream velocity outside the boundary layer (Menter *et al.*, 2006). The equation is described as follows:

$$\frac{\partial}{\partial t}(\rho\tilde{Re}_{\theta t}) + \frac{\partial}{\partial x_j}(\rho U_j \tilde{Re}_{\theta t}) = P_{\theta t} + \frac{\partial}{\partial x_j}\left[\sigma_{\theta t}\left(\mu + \mu_t\right)\frac{\partial \tilde{Re}_{\theta t}}{\partial x_j}\right] \tag{4}$$

where $P_{\theta t}$ is the source term.

The authors calibrated their transition equations to be used with the two-equation strictly empirical basis Shear-Stress Transport (SST) $k$-$\omega$ model. The underlying concept of this turbulence model is to employ a blending function to switch between the original $k$-$\omega$ model, activated in the near-wall region, and the standard $k$-$\epsilon$ model, activated in the outer wake region and free shear layers. Furthermore, the formulation of the eddy viscosity is modified to account for transport effects, including the significant influence of the principal turbulent shear stress, which enhances the prediction of aerodynamic applications (Menter, 1994). The coupling of the $\gamma$-$Re_\theta$ and $k$-$\omega$ SST models results in the Transition SST, a 4-equation turbulence model in which the intermittency function is used to activate the production term of turbulent kinetic energy downstream of the transition point (Menter *et al.*, 2006). The resulting equations are given as follows:

$$\frac{\partial}{\partial t}(\rho k) + \frac{\partial}{\partial x_i}(\rho k u_i) = \frac{\partial}{\partial x_j}\left(\Gamma_k \frac{\partial k}{\partial x_j}\right) + \gamma_{eff}\tilde{G}_k - min\left[max\left(\gamma_{eff}, 0.1\right), 1.0\right]Y_k + S_k \tag{5}$$

$$\frac{\partial}{\partial t}(\rho \omega) + \frac{\partial}{\partial x_i}(\rho \omega u_i) = \frac{\partial}{\partial x_j}\left(\Gamma_\omega \frac{\partial \omega}{\partial x_j}\right) + G_\omega - Y_\omega + D_\omega + S_\omega + G_{\omega b} \tag{6}$$

where $u_i$ is the velocity vector, $k$ is the turbulent kinect energy, $\omega$ is the specific dissipation ratio, $\Gamma_k$ and $\Gamma_\omega$ represent the effective diffusivity of $k$ and $\omega$, respectively, $\gamma_{eff}$ is the effective intermittency, $\tilde{G}_k$ and $G_\omega$ represent the production term of $k$ and $\omega$, respectively, $Y_k$ and $Y_\omega$ represent the dissipation due to turbulence of $k$ and $\omega$, respectively, $D_\omega$ is the cross-diffusion term, $S_k$ and $S_\omega$ are user-defined source terms and $G_{\omega b}$ accounts for the buoyancy term.

The turbulent intensity decay can be calculated as follows:

$$Tu = \left\{ Tu_{inlet}^2 \left[1 + \frac{3\rho V x \beta (Tu_{inlet}^2)}{2\mu(\mu_t/\mu)_{inlet}}\right]^{\frac{-\beta^*}{\beta}} \right\}^{0.5} \tag{7}$$

where $T_{u_{inlet}}$, $V$ and $(\mu_t/\mu)_{inlet}$ are the values at inlet of turbulence intensity, mean convective velocity and turbulent viscosity ratio (represented with dynamic viscosity), respectively. $\beta$ and $\beta^*$ are freestream model constants. For further details, refer to Menter *et al.* (2006), Menter (1994) and ANSYS (2021).

### 3.2 Validation

The Transition SST model was validated in the current research using the S1223 airfoil profile at $Re = 3{\cdot}10^5$. The experimental wind tunnel data is provided by Selig *et al.* (1995). The curvature correction option will be enabled with $CCURV = 1$ in order to consider the curvatures of the streamlines (Spalart and Shur, 1997).

The domain geometry was designed in SOLIDWORKS® 2019 software with a C-type topology, where the distance from the leading edge of the airfoil to the semicircular inlet is $19c$, and both the height and trailing edge distance to the outlet are set to $40c$ (Fig. 2a). Hübbe (2017) conducted his thesis using a domain with dimensions of $15c$ upstream, $20c$ downstream, and $30c$ in height, obtaining results in good agreement with wind tunnel data from McGhee *et al.* (1988) and Selig *et al.* (1995). Therefore, the dimensions adopted here were considered sufficient.

The grid strategy for high-curvature profiles was inspired by the work of Zohary *et al.* (2021). Using Ansys® ICEM CFD 2021 R2, a curvilinear and quadrilateral mesh was generated by structuring the blocks based on guide curves and outer shells created from offsets of the airfoil contour. Four outer shells were created and spaced at distances of $0.02c$, $0.10c$, $0.30c$, and $0.70c$ from the original contour, as shown in Fig. 2b. The closest shell enables control over the number of elements near the wall, both in the normal direction to the surface, due to its subdivision with perpendicular lines to the airfoil, and in the tangential direction. The remaining grid is generated based on these elements, with a geometric growth ratio of approximately 1.05 immediately after the trailing edge region to capture the near wake and 1.10 for the rest of the domain. A mesh with the dimensionless wall distance ($y^+$) set to 1 was used for the case (Fig. 2c) and the independence test that led to this choice can be observed in the next subsection (3.3Fig. 5a).

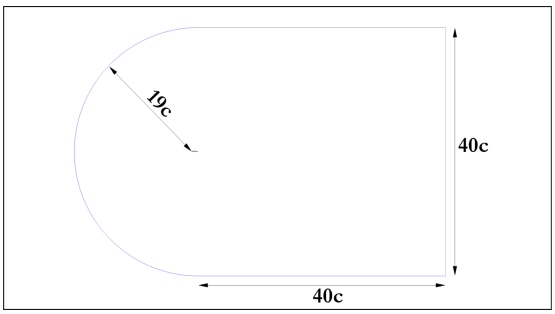


(a) C-type topology

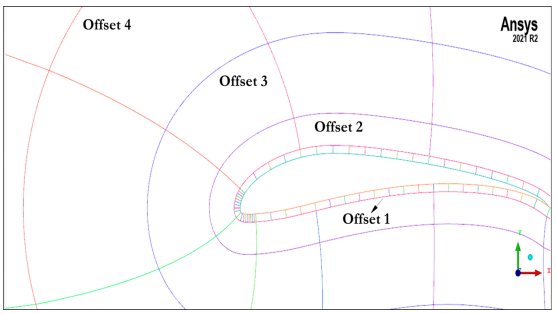


(b) Mesh structure

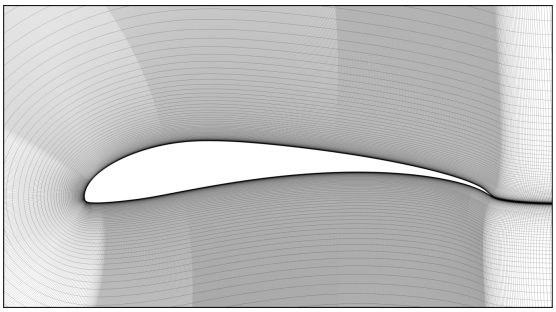

(c) S1223 validation mesh ($y^+ = 1$)

Figure 2: Computational domain (a), discretization strategy (b) and selected mesh (c)

The boundary conditions include a velocity inlet, where the components were varied to perform different angles of attack, and a pressure outlet with a static pressure set to zero. The airfoil surfaces were set as stationary walls. The experimental data was obtained using ambient values of $Tu$ lower than $0.1\%$ (Selig *et al.*, 1995). In order to achieve such a value near the airfoil profile, $Tu_{inlet}$ was set to $0.1\%$ with a $(\nu_t/\nu)_{inlet}$ value of 5, resulting in a $Tu$ value of $0.0936\%$ at the leading edge (Eq. (7)), being also consistent with the recommendation made by Spalart and Rumsey (2007).

The simulations were conducted using a pressure-based solver in a steady-state regime, with property gradients calculated by the Least Squares Cell Based method and Second-Order interpolation scheme for pressure. To ensure calculation stability, the convergence strategy steps as proposed by Hübbe (2017) were employed, involving modifications to the pressure-velocity coupling and other spatial discretizations not mentioned. Initially, 300 iterations were performed with First Order Upwind spatial discretizations and a SIMPLE pressure-velocity coupling scheme, followed by 2 000 iterations with a transition from SIMPLE to the Coupled algorithm. Finally, 10 000 iterations were completed using the Coupled scheme in combination with Second Order Upwind spatial discretizations.

The XFOIL code (Drela, 1989) was used to estimate an initial value for the stall angle (200 nodes, $\tilde{n}_{crit} = 8.3$).

Subsequently, the range of $\alpha$ values calculated by Ansys® Fluent extended from 0° to 16°, with the upper limit set to two angles beyond the preliminary $C_{l_{max}}$ angle provided by XFOIL. Convergence criteria were set as residuals below $10^{-6}$ in conjunction with variations in the coefficients of interest below $10^{-4}$. The results are presented in Fig. 3, displayed next.

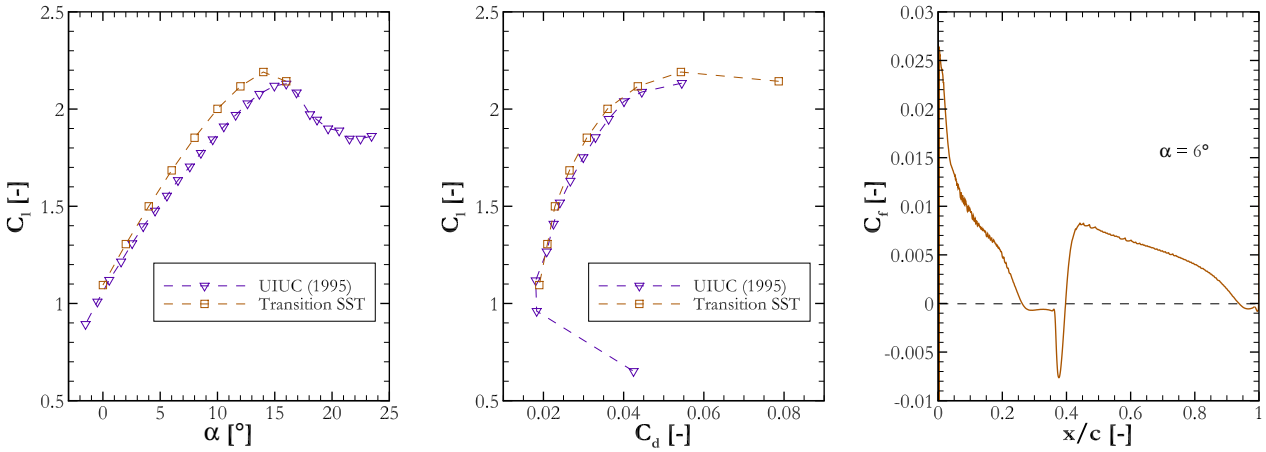


(a) $C_l \times \alpha$ (b) $C_l \times C_d$ (c) $C_f$ along the suction side.

Figure 3: Validation results for the S1223 airfoil at $Re = 3{\cdot}10^5$.

Figure 3c presents the variation of $C_f$ along the chord, indicating the position where boundary layer separation occurs ($C_f$ becomes negative) and its reattachment (returns to a positive value). Analyzing the suction side of the airfoil in Fig. 4 it can be observed that the production of turbulent kinetic energy $k$ (Fig. 4b), triggered by the intermittency $\gamma$ (Fig. 4a), occurs while the boundary layer is still separated, thus confirming the separation-induced transition and the formation of the LSB.

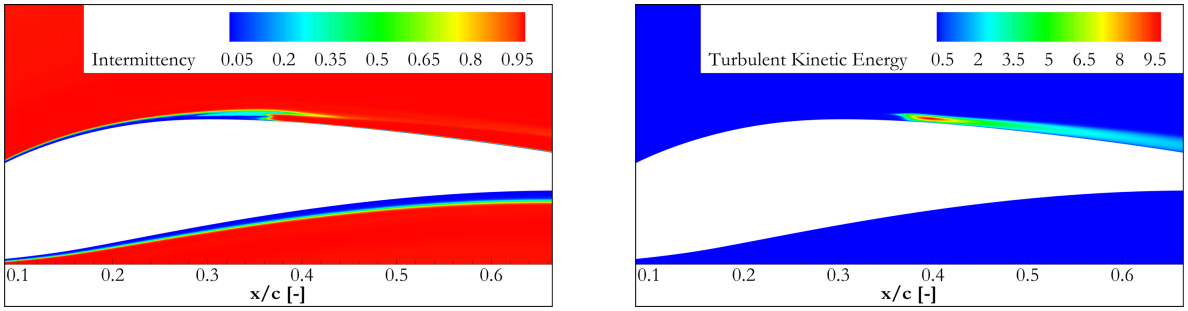


(a) Inttermitency $\gamma$ along the chord $(x/c)$. (b) Turbulent kinect energy $k$ along the chord $(x/c)$.

Figure 4: Separation-induced transition.

### 3.3 Grid independence test

Once the model is validated for the applied numerical settings, four meshes were generated based on the characteristic first cell height for each $Re$ of interest to be studied ($3{\cdot}10^5$, $4{\cdot}10^5$ and $8{\cdot}10^5$) for each airfoil. According to the Ansys® Fluent Theory Guide (ANSYS, 2021), there are minimal changes in the solution when $y^+$ values range from 0.001 to 1 for a flat plate case, and once it exceeds 8, the transition onset location begins to move upstream. The $y^+$ values chosen for this independence study were 0.1, 0.5, 1, and 5. Following the grid independence test conducted by Hübbe (2017), the total number of cells increases as the first cell adjacent to the wall is refined, i.e., as the $y^+$ value decreases. Inverted profiles were used in the meshes not intended for validation.

Critical situations of instability should be chosen for testing, as if the mesh is refined enough to simulate under such conditions, it will perform well in milder cases. The long LSB with further turbulent separation at $\alpha = 2°$ and the post-stall situation occurring beyond the provided $C_{l_{max}}$ angle given by XFOIL were the selected cases. The plots on Fig. 5 show a few examples of the obtained results.

The independence tests at $\alpha = 2°$ showed no significant discrepancies in results between the grids, as well as the tests that used $C_l$ as a comparison criterion. For both selected cases and across all tested $Re$, the coarser grids exhibited a maximum variation of 3.04% compared to the finer ones, a difference deemed negligible in this study.

As depicted in Figs. 5a and 5b, the $y^+ = 5$ grids for both airfoils exhibit a notable variation in $C_d$ when compared

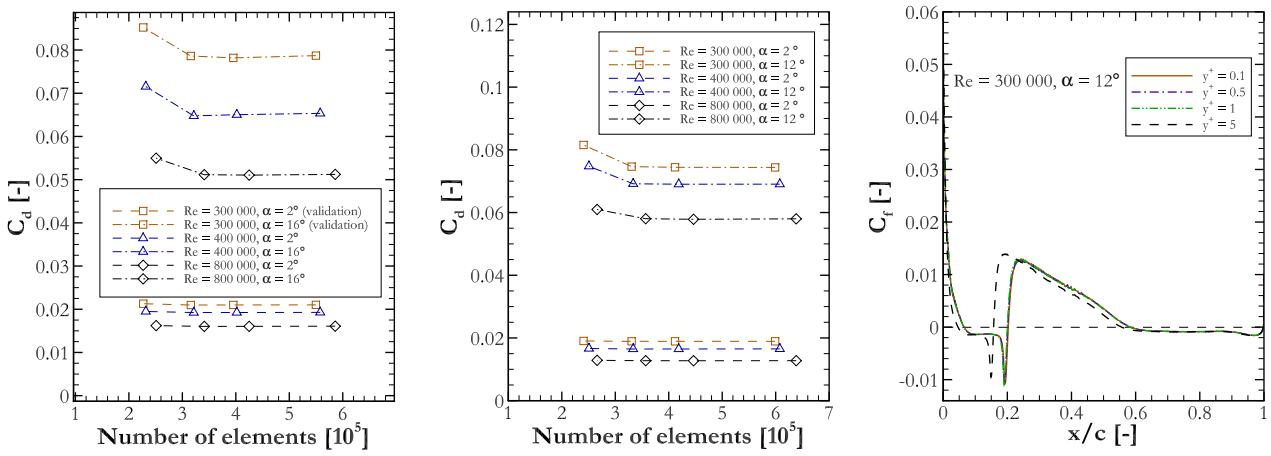


(a) $C_d$ (S1223) (b) $C_d$ (Be122-125 (c) $y^+$ influence on $C_f$ (Be122-125).

Figure 5: Grid independence tests results examples.

to the finer grid in post-stall simulated scenarios. This variation ranges between 7.33% and 9.51% for the S1223 airfoil and between 5.15% and 9.63% for the Be122-125 airfoil. Notably, it is only from the $y^+$ = 1 grid onwards that such differences become negligible, with variances of less than 0.88%.

It was also observed that, for all analyzed $Re$ and both airfoils, the coarser grids tend to predict the LSB onset earlier in post-stall situations, while the remaining grids show nearly coincident curves, as exemplified in Fig. 5c. The differences in the onset of laminar separation, when compared to the finer grid , are approximately $0.02c$ for $Re$ values of $3{\cdot}10^5$ and $4{\cdot}10^5$, and $0.01c$ for $8{\cdot}10^5$. Although such variations may seem insignificant, they will undergo a more in-depth analysis in the following section. Therefore, the $y^+$ = 1 grids were chosen for the computation of the final results.

## 4. RESULTS

First, an analysis of $C_l$ and $C_d$ were conducted for the chosen airfoils with the obtained results presented in the following figures.

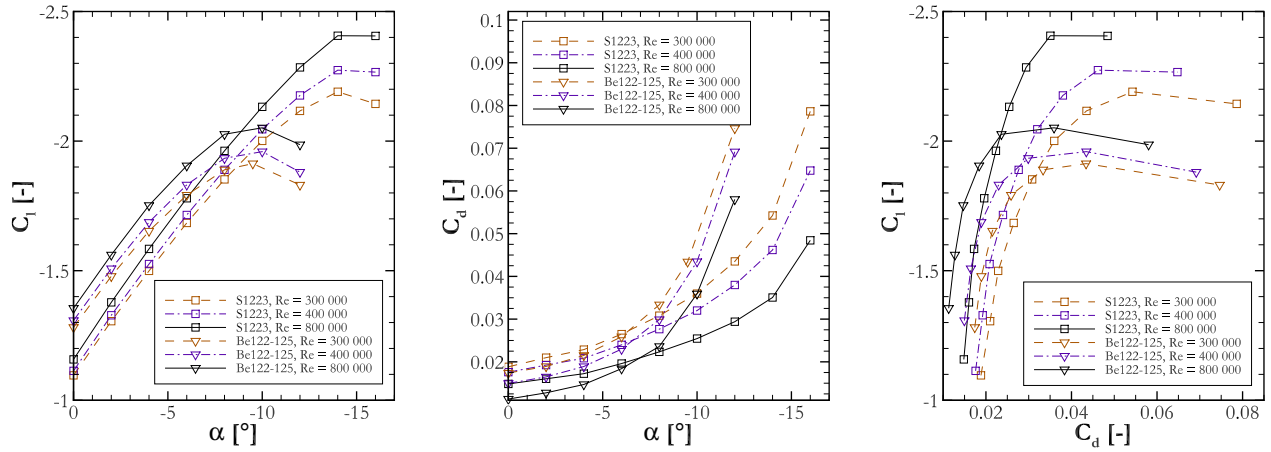


(a) $C_l \times \alpha$ (b) $C_d \times \alpha$ (c) $C_l \times C_d$

Figure 6: Validation results for the S1223 airfoil at $Re = 3{\cdot}10^5$.

For all simulated $Re$ values, the S1223 airfoil exhibited the highest $C_{l_{max}}$ (Fig. 6a), with values of 2.190 at $Re$ = $3{\cdot}10^5$, 2.274 at $Re = 4{\cdot}10^5$, and 2.406 at $Re = 8{\cdot}10^5$. In contrast, simulations for the Be122-125 airfoil yielded values of 1.831, 1.880, and 1.986 for the same $Re$ cases, respectively. Its superiority is further reaffirmed in aerodynamic efficiency ($C_l/C_d$) in the vicinity of the angle of interest, with virtually no negative slope values even at the post-stall condition at $Re$ of $4{\cdot}10^5$ and $8{\cdot}10^5$ (Fig. 6c).

The comparison illustrated in Fig. 7 reveals a higher suction peak for the S1223 airfoil in the inviscid distribution already. Although the LSB formation has a more pronounced impact on the pressure distribution on the suction side of the airfoil, the results corroborate that these viscous effects were not sufficient to make it less efficient than the Be122-125

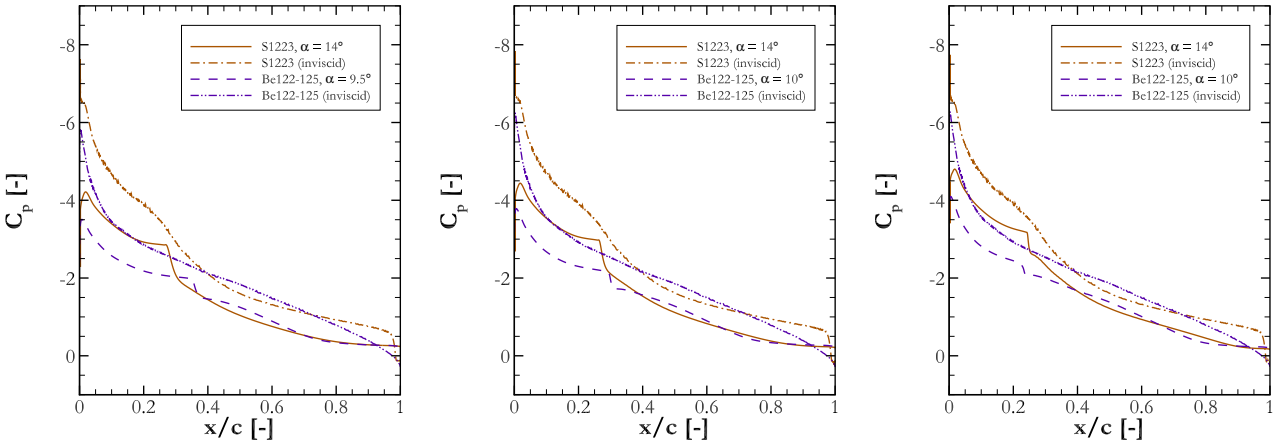


(a) $Re = 3{\cdot}10^5$. (b) $Re = 4{\cdot}10^5$. (c) $Re = 8{\cdot}10^5$.

Figure 7: $C_p$ distribution on the suction side of S1223 and Be122-125 airfoils.

airfoil.

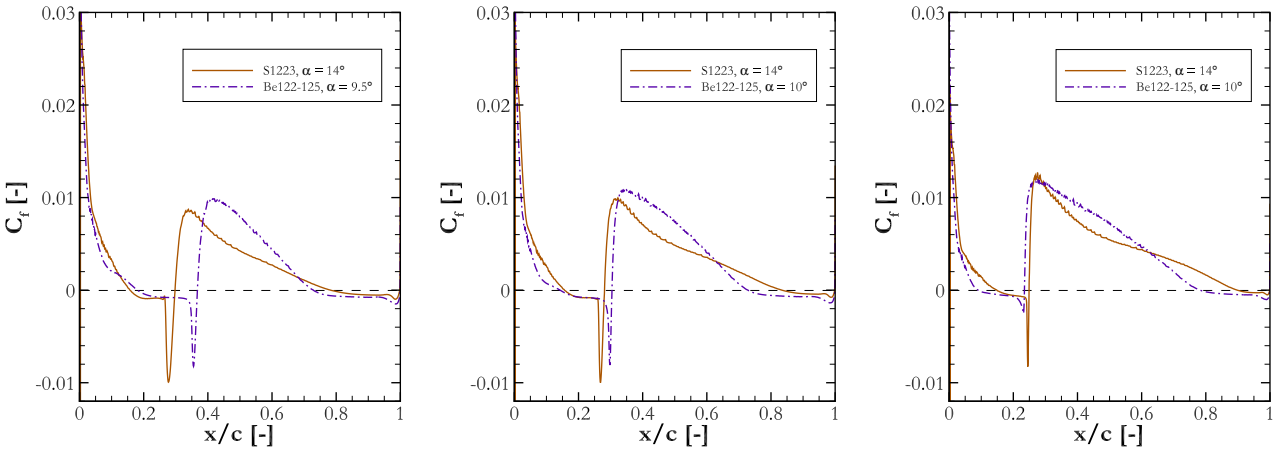


(a) $Re = 3{\cdot}10^5$. (b) $Re = 4{\cdot}10^5$. (c) $Re = 8{\cdot}10^5$.

Figure 8: $C_f$ on the suction side of S1223 and Be122-125 airfoils.

As introduced earlier, both airfoil profiles fall within a category characterized by soft stall behaviors, involving turbulent separation occurring nearer to the trailing edge. Such surface separation at $C_{l_{max}}$ angles occurs for the S1223 at positions $0.78c$ ($Re = 3{\cdot}10^5$), $0.83c$ ($Re = 4{\cdot}10^5$), and $0.90c$ ($Re = 8{\cdot}10^5$), while for the Be122-125 it occurs at $0.73c$ for the first two $Re$ values and at $0.78c$ for the last, respectively (Fig. 8). Therefore, the Be122-125 airfoil tends to exhibit an abrupter stall, as confirmed in Fig. 6a.

Excluding cases where it is possible to alter the wing's angle of attack during the race through drag reduction systems (DRS), velocity represents the primary variable in this kind of flow. Since the profiles individually exhibit nearly the same $C_{l_{max}}$ angle for all simulated $Re$ values, a comparison can be drawn to assess how the variation in velocity influences their respective performances. Figure 8 also illustrates that the Be122-125 airfoil exhibits a higher rate of transition point movement towards the leading edge, varying approximately $0.12c$. This reafirms its steeper stall compared to the S1223 profile, which transition point varies only $0.03c$ for the same $Re$ range.

## 5. CONCLUSION

Although the Be122-125 airfoil is designed with a focus on automotive racing performance, the S1223 outperformed it in all criteria presented here. The difference in the $C_{l_{max}}$ values alone would be sufficient reason for choosing the S1223 profile, as they are greater by 14.5% ($Re = 3{\cdot}10^5$), 16% ($Re = 4{\cdot}10^5$), and 17.3% ($Re = 8{\cdot}10^5$) than those obtained by the Be122-125 under the same conditions, at their respective $C_{l_{max}}$ angle.

Furthermore, the Be122-125 airfoil exhibited a higher rate of transition point movement towards the leading edge, indicating its greater sensitivity to variations in $Re$ within the range experienced in the competition dynamic events

scenarios and, consequently, an abrupter stall than the S1223. Given that peak performance is tied to the $C_{l_{max}}$ angle, it becomes crucial for the selected airfoil to be used in the aerodynamic package to maintain stability in its $C_l$ generation. Therefore, the S1223 airfoil is the most suitable choice for a low Reynolds competition such as Formula SAE.

## 6. ACKNOWLEDGEMENTS

The authors would like to thank to the Federal University of Technology - Paraná for granting the use of the Computational Research Laboratory, without which this current work would not have been possible.

## 7. REFERENCES

ANSYS, I., 2021. *Ansys® Fluent Theory Guide 2021 R2*.

Benzing, E., 1991. *Ali Wings*. Automobilia, Milan.

Drela, M., 1989. "XFOIL: An Analysis and Design System for Low Reynolds Number Airfoils". In T.J. Mueller, ed., *Low Reynolds Number Aerodynamics*. Springer Berlin Heidelberg, Berlin, Heidelberg, pp. 1–12.

Gad-el Hak, M., 1990. "Control of low-speed airfoil aerodynamics". *AIAA Journal*, Vol. 28, No. 9, pp. 1537–1552.

Hübbe, G.B.B., 2017. *Análise Numérica e Experimental de um Aerofólio de Alta Sustentação em Baixos Números de Reynolds*. Master's thesis, Universidade Federal de Santa Catarina, Florianópolis.

Liebeck, R., 1990. "Subsonic airfoil design". *American Institute fo Aeronautics and Astronautics*, Vol. 125, pp. 501–530.

McGhee, R., Walker, B.S. and Millard, B.F., 1988. "Experimental results for the Eppler 387 airfoil at low Reynolds numbers in the Langley low-turbulence pressure tunnel". Langley Research Center.

Mckay, N. and Gopalarathnam, A., 2002. "The effects of wing aerodynamics on race vehicle performance". *SAE Technical Paper No. 2002-01-3294*.

Menter, F.R., 1994. "Two-equation eddy-viscosity turbulence models for engineering applications". *AIAA Journal*, Vol. 32, No. 8, pp. 1598–1605.

Menter, F.R., Langtry, R.B., Likki, S.R., Suzen, Y.B., Huang, P.G. and Völker, S., 2006. "A correlation-based transition model using local variables — Part I: Model formulation". *Journal of Turbomachinery*, Vol. 128, No. 3, p. 413.

Pakkam, S.S., 2011. *High Downforce Aerodynamics for Motorsports*. Master's thesis, North Carolina State University, Raleigh, North Carolina.

Roberts, W.B., 1980. "Calculation of laminar separation bubbles and their effect on airfoil performance". *AIAA Journal*, Vol. 18, No. 1, pp. 25–31.

SAE International, 2022. *Formula SAE® Rules 2023 Version 2.0*. Society of Automotive Engineers.

Selig, M.S. and Guglielmo, J.J., 1997. "High-lift low reynolds number airfoil design". *Journal of Aircraft*, Vol. 34, No. 1, pp. 72–79.

Selig, M.S., Guglielmo, J.J., Broeren, A.P. and Giguere, P., 1995. *Summary of low speed airfoil data*. SoarTech Publications.

Spalart, P. and Rumsey, C., 2007. "Effective inflow conditions for turbulence models in aerodynamic calculations". *AIAA Journal*, Vol. 45, pp. 2544–2553.

Spalart, P. and Shur, M., 1997. "On the sensitization of turbulence models to rotation and curvature". *Aerospace Science and Technology*, Vol. 1, No. 5, pp. 297–302.

Wortmann, F., 1973. "A critical review of the physical aspects of airfoil design at low mach numbers". NASA CR2315.

Zohary, A.C., Asrar, W. and Aldheeb, M., 2021. "Numerical investigation on the pressure drag of some low-speed airfoils for UAV application". *CFD Letters*, Vol. 13, No. 2, pp. 29–48.

## 8. RESPONSIBILITY NOTICE

The authors are solely responsible for the printed material included in this paper.